Nanoscale

PAPER

Tumor necrosis factor interaction with gold nanoparticles†

De-Hao Tsai,[a] **Sherrie Elzey,**[a] **Frank W. DelRio,**[a] **Athena M. Keene,**[b] **Katherine M. Tyner,**[b]
Jeffrey D. Clogston,[c] **Robert I. MacCuspie,**[a] **Suvajyoti Guha,**[ad] **Michael R. Zachariah**[ad]
and Vincent A. Hackley[*a]

We report on a systematic investigation of molecular conjugation of tumor necrosis factor-α (TNF) protein onto gold nanoparticles (AuNPs) and the subsequent binding behavior to its antibody (anti-TNF). We employ a combination of physical and spectroscopic characterization methods, including electrospray-differential mobility analysis, dynamic light scattering, polyacrylamide gel electrophoresis, attenuated total reflectance-Fourier transform infrared spectroscopy, fluorescence assay, and enzyme-linked immunosorbent assay. The native TNF used in this study exists in the active homotrimer configuration prior to conjugation. After binding to AuNPs, the maximum surface density of TNF is (0.09 ± 0.02) nm^{-2} with a binding constant of 3×10^6 (mol L^{-1})$^{-1}$. Dodecyl sulfate ions induce desorption of monomeric TNF from the AuNP surface, indicating a relatively weak intermolecular binding within the AuNP-bound TNF trimers. Anti-TNF binds to both TNF-conjugated and citrate-stabilized AuNPs, showing that non-specific binding is significant. Based on the number of anti-TNF molecules adsorbed, a substantially higher binding affinity was observed for the TNF-conjugated surface. The inclusion of thiolated polyethylene glycol (SH–PEG) on the AuNPs inhibits the binding of anti-TNF, and the amount of inhibition is related to the number ratio of surface bound SH–PEG to TNF and the way in which the ligands are introduced. This study highlights the challenges in quantitatively characterizing complex hybrid nanoscale conjugates, and provides insight on TNF–AuNP formation and activity.

1. Introduction

The protein tumor necrosis factor-α (TNF) is the prototypical member of a pro-apoptotic ligand family with substantial significance for cancer therapy.[1–11] Studies show that after binding with specific cytokine receptors (TNFR) on the tumor endothelial vascular lining, TNF is able to induce hemorrhagic necrosis of several types of tumors.[8,10] However, TNF is also a known pro-inflammatory cytokine that regulates immune response. Hence potential side effects when introducing active TNF into biological systems are expected, raising concerns about its safe use and restricting its applications in cancer therapies.[1]

The benefit of targeted drug delivery, greatly facilitated by the use of nanoengineered platforms, is to mitigate these potential side effects by reducing interaction with healthy tissue. To improve therapeutic efficacy without increasing toxicity to healthy tissue, the principal approach is to increase the targeting selectivity of the drug vector toward tumor cells. This is one of the principal advantages of using nanoengineered platforms, which can accommodate multiple modalities to avoid reticulo-endothelial system (RES) removal and improve both active and passive targeting.[11,12] Recent studies indicate a promising route by conjugating TNF to a gold nanoparticle (AuNP)-based platform.[1,5,6,13–15] The general concept is to improve the transportability of TNF by immobilizing TNF onto the surface of AuNPs before binding to TNFR. Theoretically, this AuNP-based targeted drug delivery should reduce the diffusion loss and also substantially enhance the drug specificity and uptake, thus increasing intracellular concentrations for targeted cells and thereby reducing both the required dose and the corresponding collateral damage to healthy tissue.

Due to rapid uptake and clearance of AuNP–TNF by the RES,[6] thiolated polyethylene glycol (SH–PEG) is introduced into the formulation providing improved hydrophilicity while increasing residence time in the circulatory system.[6] The altered biodistribution correlates to improvements in both drug safety

[a] National Institute of Standards and Technology, Material Measurement Laboratory, Gaithersburg, MD 20899-8520, USA. E-mail: vince.hackley@nist.gov

[b] Food and Drug Administration, Center for Drug Evaluation and Research, Silver Spring, MD, 20993, USA

[c] Nanotechnology Characterization Laboratory, Advanced Technology Program, SAIC-Frederick, Inc., NCI-Frederick, Frederick, MD 21702, USA

[d] University of Maryland, Departments of Mechanical Engineering and Chemistry, College Park, MD, 20740, USA

and dose-to-dose efficacy of TNF treatment, providing proof of concept for the use of the AuNPs in targeted drug delivery for tumor eradication.

While the nanoengineered platform concept is promising, and clinical studies support the efficacy of this approach,[4,16–18] from a drug development perspective, the capacity to quantify the composition of molecular species immobilized on the surface of the carrier particles (as well as their underlying binding affinities) is critical for optimizing performance.[19] Of equal importance, the reliability of the measurement methods used to characterize the drug-particle conjugate must be considered, particularly in light of regulatory oversight. With regards to drug dose and activity, ligand surface density and conformation are useful targets for characterization, as they are indicators of therapeutic performance.[20–23] Ideally, a standardized direct molecular characterization approach would be preferred, in the same manner currently applied to small-molecule drugs; however, for nanoparticle (NP)-based therapies, the presence of the particle and the close proximity of multiple immobilized ligands create a substantially more complex and challenging analytical problem.[19] Furthermore, standardized and widely adopted characterization methods do not yet exist for NP-based materials.

By contrast, the binding of proteins and other ligands on flat surfaces, and their associated conformational changes, have been thoroughly investigated using a wide range of methods,[24–33] including attenuated total reflectance (ATR) based spectroscopies, atomic force microscopy, circular dichroism (CD), surface enhanced Raman spectroscopy (SERS), quartz crystal microbalance (QCM), and ellipsometry, among others. Some of these techniques have also found application in the study of ligand–NP interactions, in particular CD,[34,35] SERS,[36,37] QCM,[38] ATR-Fourier transform infrared (FTIR)[21,39,40] spectroscopy and ATR-fluorescence spectroscopy.[41]

Beyond these, a wide range of both traditional and novel methods have been used to probe the interaction between NPs and various ligands, both qualitatively and quantitatively. For example, UV-Vis absorbance has been used to estimate the size-dependent surface packing density of bovine serum albumin (BSA) on AuNPs,[42] and to measure the adsorption isotherm for lysozyme on SiO_2 NPs.[43] Fluorescence assays have been developed to quantify the surface packing density and binding constant for BSA on AuNPs.[21,44] Use of fluorescent labels for quantification of bound ligands is a common practice,[45] while fluorescence quenching by noble metal NPs has been widely utilized to determine binding constants for proteins and to probe conformational changes;[24,35,46–49] for example, the residues tryptophan, tyrosine, and phenylalanine have characteristic emission lines that can be exploited. Zhou et al.[50] used ^1H magic angle spinning nuclear magnetic resonance to probe the structure of thiolated ligands on AuNPs. To quantify the thermodynamics of ligand binding and probe subtle conformational changes, isothermal titration calorimetry is uniquely advantageous.[51–53] Researchers have frequently relied on methods that measure dimensional changes of NPs following interaction with ligands, such as dynamic light scattering (DLS) and differential mobility analysis (DMA), in order to estimate the ligand coating or corona thickness or to simply confirm conjugation has taken place.[21,22,48,54–57]

Size exclusion chromatography (SEC) has proven to be a powerful and accessible tool for determining the exchange rates and affinities of proteins (as well as other ligands), both in isolated form and from plasma mixtures, on NPs.[51,58,59] SEC is particularly useful for discriminating between fast and slow dissociation kinetics in multi-ligand systems. Sodium dodecyl sulfate polyacrylamide gel electrophoresis (SDS-PAGE) is a commonplace and widely used technique for the separation of proteins eluted from NPs.[51,55,59–63] 1D and 2D SDS-PAGE can be applied in conjunction with mass spectrometry, for instance, to obtain quantitative analysis, but is subject to uncertainties stemming from the specific methodology used to separate, wash, and strip the ligand–NP conjugates prior to analysis.

In the context of PEG functionalized NP vectors for therapeutic and diagnostic applications, Jokerst et al.[20] recently captured a number of key measurement issues common to the analysis of all ligand–NP conjugates: reproducibility, NP interference, quantitative capacity of the method, ligand specificity, and the difficulty of differentiating between specific and non-specific binding. The complexity of hybrid NP platforms functionalized with multiple molecular ligands cannot be understated with respect to obtaining meaningful and quantitative results.

In the case of TNF, the monomer, with a molecular mass of 17 kDa, is composed primarily of β-sheet structures. Based on literature reports,[7,9,10] unbound (i.e., not membrane associated) TNF in solution forms stable and water-soluble 51 kDa homotrimers (i.e., assemblies of three identical monomers), which are considered biologically active and are therefore able to bind with TNFR. The homotrimer active state is, in fact, a characteristic property of the TNF family of ligands.

In contrast to unbound TNF, which has been widely studied over the past decade,[7,9,10] the structure and functionality of NP-conjugated TNF still remains relatively unexplored. Not surprisingly, the few published studies have focused principally on the synthesis and biological activity of the conjugates, whereas the quantitative physicochemical characterization aspects are fairly limited in scope. Paciotti et al.[6] reported using TNF-specific enzyme-linked immunosorbent assay (ELISA) to quantify TNF uptake onto AuNPs, estimating 400 bound TNF per AuNP (33 nm diameter). They also measured zeta potential in order to monitor saturation binding of TNF. TNF–AuNPs were subsequently conjugated with thiolated PEG, but the authors do not report quantification of bound PEG nor do they discuss the potential displacement of TNF when thiolated PEG is added to the AuNP vector. In a subsequent paper, Paciotti et al.[15] describe the addition of a thiolated form of the chemotherapy agent paclitaxel to the AuNP–TNF–PEG conjugate, forming a three-component ligand system. Commercially available ELISA kits were used to quantify mass saturation binding curves for both paclitaxel and TNF. The stoichiometry derived from their analysis yielded 16 TNF and 1300 paclitaxel ligands per AuNP (25 nm diameter). More recently, Messerschmidt et al.[64] investigated single-chain TNF functionalized lipid coated polymer NPs. According to the authors, scTNF is a TNF derivative that has shown improved stability and tumoricidal response relative to the trimeric TNF.[65] The derivative is produced by coupling three TNF monomers to two peptide linkers, and was further modified with a cysteine residue to facilitate site binding to amine functionalized polymeric NPs. A

stoichiometry of 40 TNF per NP was reported through an indirect measurement: subtracting the amount of unbound TNF from the total quantity added in the formulation. This approach works well when used to determine the adsorption isotherm of an adsorbate, but the uncertainty increases with increasing adsorbate concentration.

In the present work, we summarize the findings of a systematic investigation of the interactions between TNF, antibodies (anti-TNF), SH–PEG, and AuNPs conducted using multiple physical and spectroscopic characterization methods, including DLS, electrospray-differential mobility analysis (ES-DMA), SDS-PAGE, ATR-FTIR, ELISA, and fluorescence assay. Initially, unbound TNF is characterized in solution, prior to conjugation with AuNPs. Subsequently, the adsorption and conformation of TNF on AuNPs (one-component adsorption), anti-TNF on TNF-conjugated AuNPs (two-component adsorption), and SH–PEG and anti-TNF on TNF-conjugated AuNPs (three-component adsorption) are investigated. The combination of complementary and orthogonal characterization methods provides an improved understanding of the binding mechanisms for this important therapeutic system and defines a general approach for the characterization of protein–multimer conjugate systems.

2. Experimental section

2.1 Materials

Commercially available 60 nm citrate-stabilized monodisperse colloidal AuNPs were obtained from Ted Pella Inc. (Redding, CA, USA).[66] Recombinant human TNF-α and polyclonal anti-human TNF-α (PeproTech, Rocky Hill, NJ, USA) were utilized at concentrations up to 100 μmol L^{-1} without further purification. For sample preparation of protein-conjugated AuNPs, 200 μL of aqueous solution with concentrations ranging from (0 to 28) μmol L^{-1} were first prepared and then mixed with 800 μL of AuNP suspension. The final mass concentration of AuNPs in solution was estimated to be $\approx$ 41 mg L^{-1}.[67] After 24 h, unbound ligands were removed via a centrifugation cleaning process. 20 kDa thiolated polyethylene glycol (SH–PEG20K, Nanocs, New York, NY, USA) was used at a concentration of 1 mmol L^{-1}. Sodium dodecyl sulfate (SDS, 99%, Alfa Aesar, Ward Hill, MA, USA) was used at a concentration of 35 mmol L^{-1}. Aqueous ammonium acetate (99.9%, Sigma-Aldrich, St. Louis, MO, USA) solution was prepared to adjust the ionic strength (2.5 mmol L^{-1}, 0.03 S m^{-1}). Biological grade 18.2 MΩ cm high purity deionized (DI) water (Aqua Solutions, Jasper, GA, USA) was used for preparing solutions and AuNP suspensions.

2.2 DLS and ES-DMA

DLS measurements were performed using a Zetasizer Nano (Malvern Instruments, Westborough, MA, USA). The ES-DMA system consists of an electrospray aerosol generator (Model 3480, TSI Inc., MN, USA), a differential mobility analyzer (DMA, Model 3080n, TSI Inc.) and a condensation particle counter (Model 3025, TSI Inc.). Details of the DLS and ES-DMA experimental setups and analysis have been described in previous publications.[21–23,68,69]

2.3 PAGE

PAGE was performed on Novex (4 to 20) % Tris–Glycine Mini Gels (Invitrogen, Paisley, UK). Stock protein samples (200 μg mL^{-1}) were mixed with NuPAGE lithium dodecyl sulfate (LDS) loading buffer (Invitrogen). Samples (5 μg) were electrophoresed with tris–glycine running buffer for 2 h at 125 V (EC3000P-90 Electrophoresis Power Supply, Thermo Scientific, Madison, WI). After electrophoresis, proteins were then stained with a PlusOne Silver Staining Kit (GE Healthcare, Piscataway, NJ, USA). Solutions of 2 mg mL^{-1} BSA (BioRad, Hercules, CA, USA) were used as molecular mass standards in the PAGE measurements.

2.4 Fluorescence assay and ATR-FTIR

Fluorescence assays were conducted using a Quant-iT protein assay kit (Invitrogen). A SAFIRE multi-detection monochromator microplate reader (Tecan Inc, Durham, NC, USA) was employed for the fluorescence measurements. ATR-FTIR was performed using a Nicolet Spectra 750 FTIR equipped with a Thunder Dome Germanium ATR accessory (Thermo Scientific). Details of the experimental procedures including controls for nanoparticle assay interference have been described in previous publications and are summarized in the ESI†.[21,40]

2.5 ELISA

ELISA for TNF was performed by measuring absorbance at 450 nm using a Lambda 750 double-beam UV-Vis-NIR spectrometer (Perkin Elmer, Shelton, CT, USA). AuNP samples were reacted in sequence with the components of a Human TNF-α ELISA kit (Thermo Scientific): recombinant human TNF-α, biotinylated antibody reagent, HRP-conjugated streptavidin reagent, and TMB. Details of ELISA procedures including removing the interference from AuNPs are described in the ESI†.

2.6 Measurement uncertainty

Error bars shown in figures and uncertainty ranges associated with measurement values represent one standard deviation calculated from replicate (2 to 4) measurements performed under repeatability conditions.

3. Results and discussion

3.1 TNF prior to adsorption

Due to the complexity of TNF structures, it is necessary, as a benchmark, to characterize the unbound TNF in the solution phase prior to conjugation with AuNPs. For this purpose, we utilized ES-DMA, which has been previously used as an effective tool for characterizing the molecular mass (M_m) distribution of unbound proteins.[70–73] From the measured values of M_m, the aggregation state of TNF in solution was determined. As shown in Fig. 1a, we observed a narrow M_m-distribution: the peak M_m of TNF was measured at 47.3 kDa and the full width at half maximum was about 13.2 kDa. The M_m obtained by ES-DMA is in good agreement with the reported value for free trimeric TNF.[7–9] Note that the measurement capability of ES-DMA can be as low as 6 kDa,[73] so monomeric and dimeric TNF molecules should be observable by ES-DMA if present in the system at
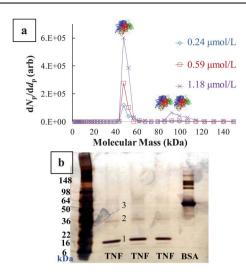
Fig. 1 Characterization of M_m-distribution of TNF prior to conjugation. (a) By ES-DMA. The dominant peak is at $M_m = 47.3$ kDa for all three C_{TNF} conditions, representing trimeric TNF. (b) By PAGE, after treating with LDS. The left most bar shows the corresponding M_m vs. measurement distance under the same electric field condition. The right most bar is the BSA internal standard. The concentration of TNF used in PAGE was 1.18 μmol L^{-1}.

detectable concentrations. The peak near 100 kDa for a TNF monomer concentration (C_{TNF}) of 1.18 μmol L^{-1} is an artifact of the electrospray process;[70–72] the probability of having two TNF trimers per droplet increases as the number concentration of TNF increases.

The mechanism of this "trimerization" is still unclear, though the major driving forces are thought to be electrostatic interactions, hydrogen bonding, hydrophobic interactions, van der Waals interactions, bridging of disulfide bonds,[8] or most likely a combination of these forces. Since the intermolecular forces within the TNF homotrimer are relatively weak compared with those of true chemical bonding,[1] it is possible to alter the trimeric conformation via changes in the environment (e.g., by pH adjustment or the addition of other ligands) and deposition (e.g., the amount of dilution) conditions. To evaluate the stability of the trimer, LDS was added to the TNF solution and analyzed by PAGE as shown in Fig. 1b. Unlike the results of Fig. 1a, the principal TNF species present following denaturization with LDS (three replicates in the middle columns) was the monomer (~17 kDa, labeled 1), with a fainter line indicative of dimers (~34 kDa, labeled 2); the trimer band (~51 kDa, labeled 3) was barely visible. The transformation from the trimer to the monomer configuration could be attributed to electrostatic repulsion from the negatively charged dodecyl sulfates adsorbed to the individual TNF monomers. The results of Fig. 1b indicate a relative weak binding affinity between monomers in trimeric TNF.
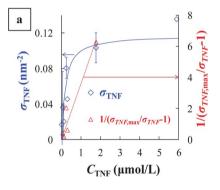
3.2 TNF on AuNPs (one-component adsorption)

After characterizing the properties of the native TNF prior to conjugation, we then determined the adsorption isotherm for TNF on AuNPs. Like other thiol containing proteins (e.g., BSA), TNF may have the capacity to bind covalently to the surface of

AuNPs through S–Au bonding;[6,21,40] however, evidence to confirm this binding mechanism is lacking and a target of current research. A protein quantification fluorescence assay was first used to measure the surface packing density of TNF (σ_{TNF}) on AuNPs. As shown in Fig. 2a, σ_{TNF} increased as C_{TNF} increased at low C_{TNF}, but eventually reached a maximum packing density of $\sigma_{TNF,max} \approx 0.11$ nm^{-2} at $C_{TNF} \approx 1.18$ μmol L^{-1}. Orthogonally, we employed ATR-FTIR to measure the adsorption isotherm of TNF on AuNPs as shown in Fig. 2b. As with the fluorescence results, σ_{TNF} initially increased with low C_{TNF}, but began to plateau at $C_{TNF} \approx 1.18$ μmol L^{-1}. In contrast, however, $\sigma_{TNF,max}$ measured by ATR-FTIR was about 40% less than the value derived from fluorescence assay. This discrepancy most likely can be attributed to differences in the measurement techniques and sample preparation (e.g., AuNPs are in suspension during fluorescence measurements and in an immobilized film during ATR-FTIR measurements).[21,40] In both cases, though, the data was well described by the Langmuir adsorption model. In this model,

$$K_{TNF-AuNP} = \frac{1}{C_{TNF}[(\sigma_{TNF,max}/\sigma_{TNF}) - 1]}, \quad (1)$$

where $K_{TNF-AuNP}$ is the equilibrium binding constant for TNF to AuNPs. As shown by the red dashed lines in Fig. 2, there was a linear relationship between $1/[(\sigma_{TNF,max}/\sigma_{TNF}) - 1]$ and C_{TNF}. From the slopes of these lines, $K_{TNF-AuNP}$ was found to vary from (2 to 4) × 10^6 (mol L^{-1})$^{-1}$. The large values for $K_{TNF-AuNP}$ indicate a high affinity for TNF on AuNPs.
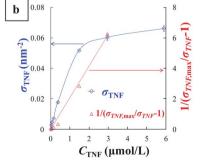

Fig. 2 Adsorption isotherms for TNF on AuNPs. Experimental temperature was 21 °C. (a) Fluorescence spectrometry. (b) ATR-FTIR. Solid lines are a guide to the eyes for the data of σ_{TNF} (diamonds). Data (triangles) are fit to Langmuir model (dashed lines). The slope of the Langmuir fit is $K_{TNF-AuNP}$.

From Fig. 2a and b, the average value for $\sigma_{TNF,max}$ was $\approx (0.09 \pm 0.02)$ nm^{-2}, based on the averaged results of fluorescence assay and ATR-FTIR. Note that σ_{TNF} is based on the number of TNF monomers per unit AuNP surface area. If the TNF was in its dimeric or trimeric form, the maximum packing density would be $\sigma_{TNF,max}/2 \approx 0.045$ nm^{-2} or $\sigma_{TNF,max}/3 \approx 0.03$ nm^{-2}, respectively. The theoretical maximum packing density $\sigma_{TNF,th}$ for each form of TNF can be calculated from the radius of gyration, r_g; $\sigma_{TNF,th} = 1/(4r_g^2)$ if each TNF group is represented as a square with sides of length $2r_g$. As shown in the ESI†, the TNF monomer, dimer, and trimer have r_g values of 1.6 nm, 2.0 nm, and 2.3 nm, which leads to saturation ratios ($\sigma_{TNF,max}/\sigma_{TNF,th}$) of 90%, 75% and 60%, respectively. As the degree of polymerization increases (from the monomer to the trimer form), $\sigma_{TNF,max}/\sigma_{TNF,th}$ decreases, suggesting that the more complex forms of TNF are more likely to occur.

As a comparison, the value for maximum packing density observed here for TNF (≈ 0.09 nm^{-2}) is about a factor of six larger than the value previously reported[21] for BSA (≈ 0.014 nm^{-2}). The differences could be due to variations in their physical size: r_g is 1.6 nm for a TNF monomer and 2.5 nm for BSA[74] (details for determining r_g are provided in the ESI†). Based on these values of r_g, the theoretical maximum surface packing density for TNF should be about a factor of three larger than that of BSA. Another possibility could be due to the difference in electrostatic repulsion from the adsorbed proteins on AuNPs. Because TNF is more neutrally charged at pH 7 compared with negatively charged BSA (the soluble form of TNF has a theoretical isoelectric point (pI) of 7.00 while BSA has a pI of 5.60),[21,75] the electrostatic repulsion between molecules should be less for TNF than for BSA, resulting in a more favorable environment to accommodate more protein in the same surface area.

After characterizing σ_{TNF} using spectroscopic methods, we then investigated the structure of TNF conjugated on AuNPs by means of two physical characterization methods: DLS and ES-DMA. Using these techniques, it is possible to quantify the physical dimensions of the TNF layer on AuNPs, as the measured increase in particle size is equal to two times the film thickness. As shown in the first column of Fig. 3a, a significant increase in the hydrodynamic particle diameter (relative to the unconjugated citrate-stabilized AuNPs) was observed by DLS ($\Delta d_{p,hz} = 10.9$ nm), corresponding to a 5.5 nm TNF shell thickness in the wet state ($0.5\Delta d_{p,hz} = 5.5$ nm). The increase in particle diameter obtained from ES-DMA, $\Delta d_{p,m}$, was determined to be 6.4 nm, corresponding to a 3.2 nm TNF shell thickness in the dry state ($0.5\Delta d_{p,m} = 3.2$ nm, first column of Fig. 3a). Because ES-DMA is a gas phase method that measures the TNF shell thickness in the dry state, the measured thickness is less than the results determined by DLS.[21,22] By comparing $0.5\Delta d_{p,hz}$ to the values of $2r_g$ for the various forms of TNF, it is possible to speculate about the conformation of TNF bound to AuNPs. From the ESI†, $2r_g$ is 3.2 nm, 4.0 nm, and 4.6 nm for the monomer, dimer, and trimer forms of TNF, respectively. Given that the measured value for $0.5\Delta d_{p,hz}$ is close to the value of $2r_g$ for the trimer, it is likely that the TNF is adopting a higher degree of polymerization on the AuNP surface. Note that we are not able to exclude the possibility that the conjugated TNF molecules are stacked in forms having an even higher degree of
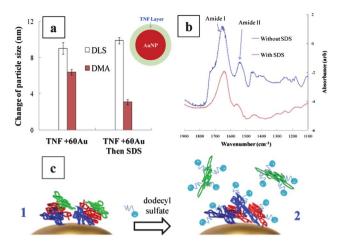

Fig. 3 Physical-based measurements of TNF conjugation with AuNPs and the effect of SDS. The TNF and SDS concentrations were 1.18 μmol L^{-1} and 3.5 mmol L^{-1}, respectively. (a) Change in particle size measured by DLS and ES-DMA. Here (TNF + 60Au then SDS) represents the condition of adding SDS subsequently to the condition of (TNF + 60Au). (b) IR spectra of TNF-conjugated AuNPs in the dry state. Background spectra represent only N$_2$. (c) Cartoon depiction of TNF on AuNPs before SDS (part 1) and after SDS (part 2, expanded with partial dissociation from surface).

aggregation than the trimer, as $0.5\Delta d_{p,hz}$ was somewhat larger than $2r_g$ for the TNF trimer. Despite the uncertainty associated with the TNF structure on the AuNP surface, we found that the width of AuNP size distribution was almost unchanged (~ 10 nm) after conjugation, indicating that TNF (in whatever form) homogeneously coated the AuNP surfaces (details on the size distributions are in the ESI†) and did not induce particle agglomeration.

To further investigate the structure of TNF and its binding to AuNPs, conjugated TNF AuNPs were subjected to SDS and then characterized by DLS and ES-DMA; SDS is used as a denaturing agent for determination of protein molecular mass. As shown in the second column of Fig. 3a (denoted as "TNF + 60Au then SDS"), $\Delta d_{p,m}$ decreased by $\approx 51\%$ after treatment with SDS, indicating a partial desorption of TNF molecules from AuNP surfaces in the dry state. ATR-FTIR was used to investigate the effect of SDS on the TNF adsorbed on AuNPs. Samples were first centrifuge-cleaned before drop-casting on the ATR crystal. Then, the ATR-FTIR measurements were performed in the dry state (details in the ESI†). Fig. 3b shows the IR spectra of TNF conjugates on AuNPs, with the two major absorption bands corresponding to TNF: amide I at ~ 1619 cm^{-1} and amide II at ~ 1510 cm^{-1}. After adding SDS, the intensities of the amide I and amide II bands decreased by at least 50%. The ATR-FTIR results confirm that a substantial quantity of the conjugated TNF is desorbed from the AuNPs. The trend shown by DLS measurements was quite different. We observe that $\Delta d_{p,hz}$ increases by 0.5 nm upon treatment with SDS; while this change is within the expected experimental uncertainty, it clearly shows that a substantial decrease in the surface coating thickness does not occur even with the corresponding loss of some surface-associated TNF. Since $\Delta d_{p,hz}$ is dependent on both molecular conformation and surface packing density,[21,22] a more expanded conformation in the presence of SDS may compensate the loss of

σ_{TNF}, resulting in a similar shell thickness. In other words, SDS may "unravel" TNF into a more extended conformation, allowing SDS and additional water molecules to fill the newly created voids. Note that the concentration of SDS used (3.5 mmol L^{-1}) was below the critical micelle concentration.

Using all of the aforementioned data, it is possible to create a hypothetical description that illustrates the various interactions between TNF and AuNPs. Prior to adding SDS (Fig. 3c, part 1), some of the TNF is directly conjugated to the AuNPs, possibly *via* covalent S–Au bonds, while other TNF molecules are attached to the AuNPs *via* non-specific interactions with neighboring conjugated TNF. After adding SDS (Fig. 3c, part 2), the TNF molecules not directly attached to the AuNPs are first denatured to a more extended form and then dissociated from the surface of the AuNPs, which results in a decrease to the measured film thickness in the dry state (decrease in $\Delta d_{p,m}$). The TNF molecules attached to the AuNP surface remain largely adsorbed, but in a more extended (denatured) conformation, resulting in an increase to the measured film thickness in the wet state (increase in $\Delta d_{p,hz}$). As stated previously, direct evidence to confirm covalent bonding between S-containing TNF and the AuNP surface is presently lacking, but S–Au bonding would be consistent with the results described above and experiments to further address this issue are planned.

3.3 Anti-TNF on TNF-conjugated AuNPs (two-component adsorption)

For applications of AuNP-based targeted drug delivery, it is vitally important to know if TNF remains active after conjugation. In this section, we use anti-TNF to determine if the binding behavior of TNF is altered after conjugation onto the AuNP surface. In solution, unbound anti-TNF has active antigen recognition sites (receptors) capable of binding with the active unbound TNF. The interaction between anti-TNF and the TNF–AuNP conjugate is relatively unexplored. For example, it is still unknown whether sub-monolayer TNF coatings would provide better accessibility to epitopes on the TNF complex that would enable anti-TNF binding, thereby increasing the percentage of conjugated TNF recognized. Our objective here was to confirm that binding between anti-TNF and TNF still occurs after TNF is surface bound. The assumption of activity for the bound TNF is based on previous evidence of antibodies being able to recognize their antigen targets when those targets were bound to nanoparticles.[76]

First we performed physical measurements to obtain dimensional information regarding anti-TNF bound to both TNF-conjugated and citrate-stabilized AuNPs (the latter serving as a de facto control). After the surface of AuNPs was fully saturated with TNF molecules (*i.e.*, the surface density reached a plateau), anti-TNF at a concentration of 0.27 μmol L^{-1} was introduced into the system. Note that at least 98% of unbound TNF was removed prior to the interaction between TNF–AuNP and anti-TNF. As shown in Fig. 4a, $\Delta d_{p,hz}$ (from DLS) and $\Delta d_{p,m}$ (from DMA) of TNF-conjugated AuNPs increased from 10.9 nm to 21.2 nm and from 6.4 nm to 11.3 nm, respectively, suggesting the formation of an anti-TNF layer on the TNF-conjugated AuNPs. Subtracting the contribution of the TNF layer discussed previously, $\Delta d_{p,hz}$ and $\Delta d_{p,m}$ from the anti-
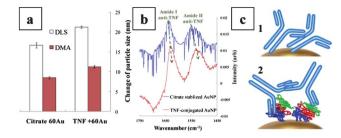

Fig. 4 Characterization of anti-TNF adsorption on AuNPs. (a) Change in particle size measured by DLS and DMA. (b) IR difference spectra of anti-TNF on citrate-stabilized AuNPs (top, blue) and TNF-conjugated AuNPs (bottom, red). The background spectrum for anti-TNF on citrate-stabilized AuNPs was determined using citrate-stabilized AuNPs in DI water, and the background spectrum for anti-TNF on TNF-conjugated AuNPs was determined using TNF-conjugated AuNPs in DI water. (c) Cartoon depiction of anti-TNF adsorption onto citrate-stabilized AuNPs (part 1) and on TNF-conjugated AuNPs (part 2).

TNF layer alone was 10.3 nm and 4.9 nm, respectively. Note that the difference between $\Delta d_{p,hz}$ and $\Delta d_{p,m}$ here is due primarily to the difference in the measurement environment as discussed previously.

We also observed that anti-TNF was able to directly adsorb to the surface of AuNPs without the presence of conjugated TNF (*i.e.*, in the absence of antigen binding receptors). As shown in Fig. 4a, we observed $\Delta d_{p,hz} = 16.7$ nm and $\Delta d_{p,m} = 8.5$ nm after the adsorption of anti-TNF on citrate-stabilized AuNPs. In this case, binding could occur *via* the cysteine or amine groups in the sequence of anti-TNF,[21,22,58,77] which is similar to other types of protein absorption on AuNPs and was not specific to the antigen binding receptors. In general, the dimensional information measured by DLS and ES-DMA in Fig. 4a is in semi-quantitative agreement. In general, $\Delta d_{p,hz}$ and $\Delta d_{p,m}$ from adsorption of anti-TNF was unexpectedly larger for the citrate-stabilized AuNPs than for the TNF-conjugated AuNPs. The difference can be attributed to either a difference in the amount of anti-TNF adsorbed on the AuNPs or to a difference in the conformation of the adsorbed anti-TNF layer in the presence and absence of the receptors. DLS and ES-DMA are unable to identify the location of the anti-TNF on the AuNPs. However, it is unlikely that the anti-TNF displaced the conjugated TNF, as the anti-TNF concentration was small ($C_{anti-TNF} < 0.05$ μmol L^{-1}) and the TNF packing density was large (*i.e.*, close to saturation).

ATR-FTIR was employed to provide spectroscopic information complementary to the dimensional analysis. As shown in Fig. 4b, the amide I and amide II peaks representing anti-TNF adsorption on both citrate-stabilized AuNPs (top, blue) and TNF-conjugated AuNPs (bottom, red) were observed after water cleaning steps, confirming that the anti-TNF was bound to the AuNPs in both cases. For the anti-TNF on citrate-stabilized AuNPs, the amide I and amide II frequencies were 1633 cm^{-1} and 1546 cm^{-1}, respectively. In contrast, the amide I and amide II frequencies for the anti-TNF on TNF-conjugated AuNPs were 1627 cm^{-1} and 1526 cm^{-1}, respectively. The shifts in characteristic absorbance peak wavenumbers suggest differences in anti-TNF conformation on the two different types of surfaces. In addition, from the change of vibration frequency, it is reasonable

to exclude the effect of anti-TNF adsorption to the citrate-stabilized gold surface directly when σ_{TNF} is high (details in ESI†).

Using all of the aforementioned data, it is possible to describe a physical model that illustrates the two different binding mechanisms for anti-TNF on AuNPs, as shown in Fig. 4c. In the absence of TNF (Fig. 4c, part 1), anti-TNF can bind to the AuNP surface through its reactive functional groups (such as cysteines), and this type of binding mechanism shows no specificity to its antigen receptors. By contrast, on the TNF coated AuNP surface (Fig. 4c, part 2), anti-TNF preferably binds with the antigens of the TNF–AuNP conjugates (and may be sterically excluded from binding directly with the AuNP surface).

3.4 SH–PEG and anti-TNF on TNF-conjugated AuNPs (three-component adsorption)

Conceptually, SH–PEG provides the TNF–AuNP conjugate with a measure of protection from removal by the RES,[20,58] and may prevent the surface-bound TNF from being recognized by ligand receptors other than the TNFR on the tumor endothelial vascular lining.[5,6] As discussed previously, the one component adsorption to AuNPs (TNF + AuNP) shows low delivery efficacy in a published preclinical study: the drug vector was highly recognized by the RES system. Adding SH–PEG to the TNF–AuNP formulation (i.e., two component ligand system) exhibited effective reduction in RES removal.[2,4–6] Although effective in preclinical studies, there remains a lack of quantitative understanding of this phenomenon and the factors that impact it. In a previous study we demonstrated the efficacy of using ATR-FTIR to characterize competitive adsorption between a protein (BSA) and SH–PEG on AuNPs. Results indicated that the presence of SH–PEG inhibits the adsorption of BSA. In the present work, ATR-FTIR was used to assess the effect of SH–PEG on the subsequent anti-TNF binding to TNF-conjugated AuNPs (i.e., presence of both SH–PEG and TNF). Studies were performed using SH–PEG with $M_m = 20$ kDa (denoted as SH–PEG20K), as it is not easily displaced by competing proteins and has been widely used for RES avoidance in other systems.[40] Two different surface density ratios (i.e., surface density of SH–PEG20K, $\sigma_{SH–PEG20K}$, to σ_{TNF}) were prepared using the same concentration of TNF (2.9 μmol L^{-1}) and SH–PEG (200 μmol L^{-1}) but with different adsorption conditions: simultaneous competitive adsorption (denoted as Condition 1) and displacement of pre-existing TNF conjugates by SH–PEG20K (denoted as Condition 2). Details on sample preparation are given in the ESI†. Because of the effects of available binding sites on the AuNP surface, and steric hindrance,[22,40] a higher ratio of $\sigma_{SH–PEG20K}$ to σ_{TNF} was expected in Condition 1 than in Condition 2.

Fig. 5a shows the IR spectra for TNF and SH–PEG20K on AuNPs. Amide I and amide II bands were observed for all three conditions, confirming TNF adsorption. In Condition 1 and Condition 2, we observed absorption peaks at 1080 cm^{-1}, which correspond to C–O stretching of SH–PEG (denoted as (C–O)$_{PEG}$), after SH–PEG20K was adsorbed to AuNPs.[40] The surface packing densities of TNF and SH–PEG20K were calculated using the intensities of the amide II bands and the (C–O)$_{PEG}$ peaks, respectively, as shown in Fig. 5b. In Condition 1, $\sigma_{SH–PEG20K}$ and σ_{TNF} were 0.011 nm^{-2} and 0.007 nm^{-2}, respectively. In Condition 2, $\sigma_{SH–PEG20K}$ and σ_{TNF} were
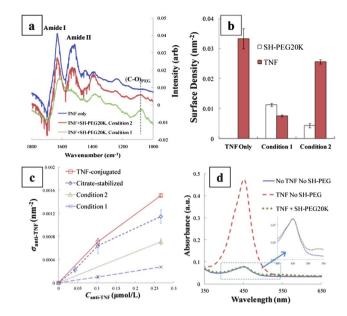

Fig. 5 Effect of SH–PEG20K on anti-TNF adsorption onto AuNPs. (a) IR spectra for TNF and (TNF + SH–PEG20K)-conjugated AuNPs. The background spectrum was citrate-stabilized AuNPs in DI water. (b) Surface densities of TNF and SH–PEG20K on AuNPs. (c) Adsorption isotherms for anti-TNF on AuNPs measured by ATR-FTIR, with and without TNF and/or SH–PEG20K. (d) ELISA results for anti-TNF conjugation on AuNPs. Conditions 1 and 2 represent different ratios of $\sigma_{SH–PEG20K}$ to σ_{TNF}. The background spectrum was DI water.

0.004 nm^{-2} and 0.026 nm^{-2}, respectively. Hence, the ratio of $\sigma_{SH–PEG20K}$ to σ_{TNF} in Condition 1 was about an order of magnitude larger than that in Condition 2. Details on the calculation of $\sigma_{SH–PEG20K}$ and σ_{TNF} were provided in a previous publication[40] and are also summarized in the ESI†.

After functionalizing with different $\sigma_{SH–PEG20K}$ to σ_{TNF} ratios, anti-TNF was introduced. The surface packing density of anti-TNF, $\sigma_{anti-TNF}$, was quantified based on the intensity of the amide II band in the corresponding ATR-FTIR spectra. As shown in Fig. 5c, $\sigma_{anti-TNF}$ increased as the concentration of anti-TNF, $C_{anti-TNF}$, increased for all conditions studied. In the range of $C_{anti-TNF}$ studied, the maximum value of $\sigma_{anti-TNF}$ (denoted as $\sigma_{anti-TNF,max}$) on TNF-conjugated AuNPs was ≈ 0.0014 nm^{-2}, which is slightly larger than that for citrate-stabilized AuNPs ($\sigma_{anti-TNF,max} \approx 0.0011$ nm^{-2}). Thus, although evidence shows that antigen binding on TNF promotes anti-TNF adsorption to AuNPs, non-specific adsorption is nonetheless substantial when TNF is absent. With SH–PEG20K on the AuNPs, $\sigma_{anti-TNF}$ decreased significantly; $\sigma_{anti-TNF,max}$ decreased by 82% for Condition 1 and 51% for Condition 2. Quantitatively, ATR-FTIR results indicate that a larger ratio of $\sigma_{SH–PEG20K}$ to σ_{TNF} creates greater inhibition to anti-TNF adsorption on AuNPs. Note that SH–PEG remains relatively stable on AuNPs after interacting with anti-TNF in our experiment.

Orthogonally, we used ELISA as a qualitative comparison to the results of ATR-FTIR shown in Fig. 5c. In the ELISA experiments, the optical response is the absorbance of horseradish peroxidase (HRP)-catalyzed tetramethylbenzidine substrate (TMB) ($\lambda = 450$ nm), which is dependent on the amount of HRP-linked streptavidin conjugated on AuNPs

through biotinylated anti-TNF. A decrease in HRP should be evident, based on the corresponding optical response, if the SH–PEG20K coating serves to screen anti-TNF adsorption. As shown in Fig. 5d, for TNF-conjugated AuNPs, a strong absorbance at $\lambda = 450$ nm was observed after allowing the HRP to catalyze reaction of TMB for 30 minutes before quenching with sulfuric acid. With SH–PEG20K on the AuNPs, the optical response decreased by about 90%, indicating the adsorption of anti-TNF on TNF-conjugated AuNPs is strongly inhibited. Note that the SH–PEG20K was introduced to AuNP simultaneously with TNF. Also, the absorbance for TNF-conjugated AuNPs was significantly larger than citrate-stabilized AuNPs alone (even though the difference seems to be more significant than the results of ATR-FTIR). The ELISA results show that the conjugated TNF molecules promote adsorption of anti-TNF onto AuNPs. The ELISA results are in qualitative agreement with ATR-FTIR measurements. Future work will seek to improve the quantitative capacity for orthogonal comparison of these two techniques.

4. Conclusions

Adsorption of TNF and anti-TNF on AuNPs can be characterized through a selective combination of physical and spectroscopic approaches. We confirmed that TNF molecules exist in the trimeric form in solution, with relatively weak intra-aggregate binding. Following conjugation, the surface adsorbed density of TNF on AuNPs approaches a plateau value ≈ 0.09 nm^{-2}. A high binding affinity was found between TNF and AuNPs, with a binding constant $K_{TNF–AuNP} \approx 3 \times 10^6$ (mol L^{-1})$^{-1}$. Anti-TNF can bind at substantial levels with both citrate-stabilized and TNF-conjugated AuNPs, suggesting that nonspecific binding occurs on the Au surface in addition to antigen specific binding. In the presence of bound SH–PEG (20 kDa), the binding of anti-TNF to TNF-conjugated AuNPs is partially inhibited due to screening and TNF displacement by the SH–PEG. This "screening" effect is lessened when TNF is first conjugated to the AuNPs and SH–PEG is added subsequently (compared with simultaneous conjugation). The coexistence of TNF and PEG on the AuNP surface is a necessary requirement for clinical applications, as each serves a specific function; however, our results demonstrate that SH–PEG can strongly inhibit TNF binding to AuNP, and so the order and relative concentrations of these species must be carefully controlled in order to obtain a clinically efficacious balance of ligands. The molar mass of the SH–PEG may also be a significant factor, though this was not explored in the present study. Shorter chain PEG ligands would likely provide a reduction in the observed TNF inhibition, but they may also impact TNF binding and drug efficacy. It is worth noting that 20 kDa PEG is at the upper end of the molar mass range typically used with NP drug delivery vectors ($\sim$1000 Da to 20 kDa),[20] though ligands with much smaller ethylene glycol monomer repeats have been reported.[78] Extension of the characterization strategy we report here to interrogate the effects of PEG chain length is an apt topic for future research. The use of molecular linkers to improve TNF conjugate stability and bioactivity, as described recently by Messerschmidt *et al.*,[64] is another promising approach that would be of particular interest from a characterization

perspective. The use of such linkers might also facilitate improved surface passivation to mitigate the high level of non-specific adsorption of TNFR observed in the present study.

Additionally, we found that the presence of AuNPs in the ELISA assay interferes with the optical detection modality. Removal of the AuNPs is not easily achieved, and can create additional uncertainties (*e.g.*, due to the recovery of ligands prior to ELISA measurements). From our experience with TNF–AuNP conjugates, ELISA is limited to qualitative analysis when conducted in the presence of AuNPs, despite the ease of measurement accessibility for such assays.

In conclusion, the work presented here provides a prototype methodology: using a combination of widely available dimensional and spectroscopic characterization methods in order to interrogate the adsorption and desorption processes in multiple ligand–nanoparticle systems. This is particularly useful where protein ligands are characterized by a complex structure (*e.g.*, a reactive trimer aggregate, as in the case of TNF). In addition, the methodology developed in this study can be applied to investigate other types of antibody–antigen interactions, as well as the potential screening effect of competing ligands present during formulation of nanoparticle-based therapeutic platforms. Although the present work is comprehensive in scope, and has provided new insight, questions regarding the mechanistic aspects of TNF binding and its surface-bound conformation remain. Future studies will include refinement of the current methodology and continued development of new approaches.

Notes and references

1 J. M. Farma, M. Puhlmann, P. A. Soriano, D. Cox, G. F. Paciotti, L. Tamarkin and H. R. Alexander, *Int. J. Cancer*, 2007, **120**, 2474–2480.
2 R. Goel, N. Shah, R. Visaria, G. F. Paciotti and J. C. Bischof, *Nanomedicine*, 2009, **4**, 401–410.
3 R. Goel, D. Swanlund, J. Coad, G. F. Paciotti and J. C. Bischof, *Mol. Cancer Ther.*, 2007, **6**, 2039–2047.

4 S. K. Libutti, G. F. Paciotti, L. Myer, R. Haynes, W. Gannon, M. Walker, G. Seidel, A. Byrnes, N. Yuldasheva and L. Tamarkin, *J. Clin. Oncol.*, 2009, **27**, 15s (suppl; abstr 3586).

5 G. F. Paciotti, D. G. I. Kingston and L. Tamarkin, *Drug Dev. Res.*, 2006, **67**, 47–54.

6 G. F. Paciotti, L. Myer, D. Weinreich, D. Goia, N. Pavel, R. E. McLaughlin and L. Tamarkin, *Drug Delivery*, 2004, **11**, 169–183.

7 R. A. Smith and C. Baglioni, *J. Biol. Chem.*, 1987, **262**, 6951–6954.

8 R. A. Smith and C. Baglioni, *J. Biol. Chem.*, 1989, **264**, 14646–14652.

9 P. Tang, M. C. Hung and J. Klostergaard, *Biochemistry*, 1996, **35**, 8216–8225.

10 R. van Horssen, T. L. M. ten Hagen and A. M. M. Eggermont, *Oncologist*, 2006, **11**, 397–408.

11 E. Bremer, M. de Bruyn, H. Wajant and W. Helfrich, *Curr. Drug Targets*, 2009, **10**, 94–103.

12 P. P. Adiseshaiah, J. B. Hall and S. E. McNeil, *WIREs Nanomed. Nanobiotechnol.*, 2010, **2**, 99–112.

13 R. K. Visaria, R. J. Griffin, B. W. Williams, E. S. Ebbini, G. F. Paciotti, C. W. Song and J. C. Bischof, *Mol. Cancer Ther.*, 2006, **5**, 1014–1020.

14 D. Harjanto, *Biological Applications*, NNIN REU 2006 Research Accomplishments, 2006.

15 G. F. Paciotti, L. Myer, D. G. I. Kingston, T. Ganesh and T. Tamarkin, *NSTI-Nanotech 2005*, www.nsti.org, 2005, vol. 1.

16 http://nano.cancer.gov/learn/now/clinical-trials.asp.

17 C. Riggio, E. Pagni, V. Raffa and A. Cuschieri, *J. Nanomater.*, 2011, DOI: 10.1155/2011/164506.

18 S. K. Libutti, G. F. Paciotti, A. A. Byrnes, H. R. Alexander, W. E. Gannon, M. Walker, G. D. Seidel, N. Yuldasheva and L. Tamarkin, *Clin. Cancer Res.*, 2010, **16**, 6139–6149.

19 S. E. McNeil, *Characterization of Nanoparticles Intended for Drug Delivery*, Springer, New York, 2011.

20 J. V. Jokerst, T. Lobovkina, R. N. Zare and S. S. Gambhir, *Nanomedicine*, 2011, **6**, 715–728.

21 D. H. Tsai, F. W. DelRio, A. M. Keene, K. M. Tyner, R. I. MacCuspie, T. J. Cho, M. R. Zachariah and V. A. Hackley, *Langmuir*, 2011, **27**, 2464–2477.

22 D. H. Tsai, F. W. DelRio, R. I. MacCuspie, T. J. Cho, M. R. Zachariah and V. A. Hackley, *Langmuir*, 2010, **26**, 10325–10333.

23 D. H. Tsai, R. A. Zangmeister, L. F. Pease, M. J. Tarlov and M. R. Zachariah, *Langmuir*, 2008, **24**, 8483–8490.

24 S. H. Brewer, W. R. Glomm, M. C. Johnson, M. K. Knag and S. Franzen, *Langmuir*, 2005, **21**, 9303–9307.

25 K. K. Chittur, *Biomaterials*, 1998, **19**, 357–369.

26 J. J. Gray, *Curr. Opin. Struct. Biol.*, 2004, **14**, 110–115.

27 C. A. N. Haynes and W. Norde, *Colloids Surf., B*, 1994, **2**, 517.

28 V. Hlady and J. Buijs, *Curr. Opin. Biotechnol.*, 1996, **7**, 72–77.

29 K. Nakanishi, T. Sakiyama and K. Imamura, *J. Biosci. Bioeng.*, 2001, **91**, 233–244.

30 P. Schon, M. Gorlich, M. J. J. Coenen, H. A. Heus and S. Speller, *Langmuir*, 2007, **23**, 9921–9923.

31 J. R. Smith, M. T. Cicerone and C. W. Meuse, *Langmuir*, 2009, **25**, 4571–4578.

32 T. J. Su, J. R. Lu, R. K. Thomas, Z. F. Cui and J. Penfold, *J. Colloid Interface Sci.*, 1998, **203**, 419–429.

33 M. Wahlgren, T. Arnebrant and I. Lundstrom, *J. Colloid Interface Sci.*, 1995, **175**, 506–514.

34 W. Shang, J. H. Nuffer, V. A. Muniz-Papandrea, W. Colon, R. W. Siegel and J. S. Dordick, *Small*, 2009, **5**, 470–476.

35 N. Wangoo, C. R. Suri and G. Shekhawat, *Appl. Phys. Lett.*, 2008, **92**, 133104.

36 K. Fujiwara, H. Watarai, H. Itoh, E. Nakahama and N. Ogawa, *Anal. Bioanal. Chem.*, 2006, **386**, 639–644.

37 C. S. Levin, S. W. Bishnoi, N. K. Grady and N. J. Halas, *Anal. Chem.*, 2006, **78**, 3277–3281.

38 E. D. Kaufman, J. Belyea, M. C. Johnson, Z. M. Nicholson, J. L. Ricks, P. K. Shah, M. Bayless, T. Pettersson, Z. Feldoto, E. Blomberg, P. Claesson and S. Franzen, *Langmuir*, 2007, **23**, 6053–6062.

39 C. L. McFearin, J. Sankaranarayanan and A. Almutairi, *Anal. Chem.*, 2011, **83**, 3943–3949.

40 D.-H. Tsai, M. Davila-Morris, F. W. DelRio, S. Guha, M. R. Zachariah and V. A. Hackley, *Langmuir*, 2011, **27**, 9302–9313.

41 C. Czeslik, G. Jackler and C. Royer, *Spectrosc.-Int. J.*, 2002, **16**, 139–145.

42 J. H. Teichroeb, J. A. Forrest and L. W. Jones, *Eur. Phys. J. E: Soft Matter Biol. Phys.*, 2008, **26**, 411–415.

43 B. Bharti, J. Meissner and G. H. Findenegg, *Langmuir*, 2011, **27**, 9823–9833.

44 L. M. Demers, C. A. Mirkin, R. C. Mucic, R. A. Reynolds, R. L. Letsinger, R. Elghanian and G. Viswanadham, *Anal. Chem.*, 2000, **72**, 5535–5541.

45 L. Maus, J. P. Spatz and R. Fiammengo, *Langmuir*, 2009, **25**, 7910–7917.

46 D. J. Gao, Y. Tian, S. Y. Bi, Y. H. Chen, A. M. Yu and H. Q. Zhang, *Spectrochim. Acta, Part A*, 2005, **62**, 1203–1208.

47 M. Iosin, F. Toderas, P. L. Baldeck and S. Astilean, *J. Mol. Struct.*, 2009, **924–26**, 196–200.

48 S. H. D. Lacerda, J. J. Park, C. Meuse, D. Pristinski, M. L. Becker, A. Karim and J. F. Douglas, *ACS Nano*, 2010, **4**, 365–379.

49 B. F. Pan, D. X. Cui, P. Xu, Q. Li, T. Huang, R. He and F. Gao, *Colloids Surf., A*, 2007, **295**, 217–222.

50 H. Y. Zhou, F. F. Du, X. Li, B. Zhang, W. Li and B. Yan, *J. Phys. Chem. C*, 2008, **112**, 19360–19366.

51 T. Cedervall, I. Lynch, S. Lindman, T. Berggard, E. Thulin, H. Nilsson, K. A. Dawson and S. Linse, *Proc. Natl. Acad. Sci. U. S. A.*, 2007, **104**, 2050–2055.

52 M. De, O. R. Miranda, S. Rana and V. M. Rotello, *Chem. Commun.*, 2009, 2157–2159.

53 M. De, C. C. You, S. Srivastava and V. M. Rotello, *J. Am. Chem. Soc.*, 2007, **129**, 10747–10753.

54 E. Casals, T. Pfaller, A. Duschl, G. J. Oostingh and V. Puntes, *ACS Nano*, 2010, **4**, 3623–3632.

55 M. A. Dobrovolskaia, A. K. Patri, J. W. Zheng, J. D. Clogston, N. Ayub, P. Aggarwal, B. W. Neun, J. B. Hall and S. E. McNeil, *Nanomed.: Nanotechnol., Biol. Med.*, 2009, **5**, 106–117.

56 N. G. Khlebtsov, V. A. Bogatyrev, B. N. Khlebtsov, L. A. Dykman and P. Englebienne, *Colloid J.*, 2003, **65**, 622–635.

57 L. F. Pease, D. H. Tsai, R. A. Zangmeister, M. R. Zachariah and M. J. Tarlov, *J. Phys. Chem. C*, 2007, **111**, 17155–17157.

58 W. Eck, G. Craig, A. Sigdel, G. Ritter, L. J. Old, L. Tang, M. F. Brennan, P. J. Allen and M. D. Mason, *ACS Nano*, 2008, **2**, 2263–2272.

59 M. Lundqvist, J. Stigler, G. Elia, I. Lynch, T. Cedervall and K. A. Dawson, *Proc. Natl. Acad. Sci. U. S. A.*, 2008, **105**, 14265–14270.

60 A. Gessner, A. Lieske, B. R. Paulke and R. H. Muller, *Eur. J. Pharm. Biopharm.*, 2002, **54**, 165–170.

61 A. Gessner, R. Waicz, A. Lieske, B. R. Paulke, K. Mader and R. H. Muller, *Int. J. Pharm.*, 2000, **196**, 245–249.

62 M. Luck, B. R. Paulke, W. Schroder, T. Blunk and R. H. Muller, *J. Biomed. Mater. Res.*, 1998, **39**, 478–485.

63 I. Lynch and K. A. Dawson, *Nano Today*, 2008, **3**, 40–47.

64 S. K. E. Messerschmidt, A. Musyanovych, M. Altvater, P. Scheurich, K. Pfizenmaier, K. Landfester and R. E. Kontermann, *J. Controlled Release*, 2009, **137**, 69–77.

65 A. Krippner-Heidenreich, I. Grunwald, G. Zimmermann, M. Kuhnle, J. Gerspach, T. Sterns, S. D. Shnyder, J. H. Gill, D. N. Mannel, K. Pfizenmaier and P. Scheurich, *J. Immunol.*, 2008, **180**, 8176–8183.

66 The identification of any commercial product or trade name does not imply endorsement or recommendation by the National Institute of Standards and Technology.

67 Reports of Investigation, Reference Materials 8011, 8012 and 8013, National Institute of Standards and Technology, http://www.nist.gov/srm/, 2008.

68 D. H. Tsai, T. J. Cho, F. W. DelRio, J. Taurozzi, M. R. Zachariah and V. A. Hackley, *J. Am. Chem. Soc.*, 2011, **133**, 8884–8887.

69 D. H. Tsai, L. F. Pease, 3rd, R. A. Zangmeister, M. J. Tarlov and M. R. Zachariah, *Langmuir*, 2009, **25**, 140–146.

70 M. Li, S. Guha, R. Zangmeister, M. J. Tarlov and M. R. Zachariah, *Langmuir*, 2011, **27**, 14732–14739.

71 M. D. Li, S. Guha, R. Zangmeister, M. J. Tarlov and M. R. Zachariah, *Aerosol Sci. Technol.*, 2011, **45**, 849–860.

72 L. F. Pease, 3rd, J. T. Elliott, D. H. Tsai, M. R. Zachariah and M. J. Tarlov, *Biotechnol. Bioeng.*, 2008, **101**, 1214–1222.

73 L. F. Pease, 3rd, M. Sorci, S. Guha, D. H. Tsai, M. R. Zachariah, M. J. Tarlov and G. Belfort, *Biophys. J.*, 2010, **99**, 3979–3985.

74 P. Narang, K. Bhushan, S. Bose and B. Jayaram, *J. Biomol. Struct. Dyn.*, 2006, **23**, 385–406.

75 Swiss Institute of Bioinformatics, ExPASy Bioinformatics Resource Portal (http://web.expasy.org/compute_pi/); UniProt Knowledgebase, UniProt Consortium (http://www.uniprot.org), primary accession numbers P01375 and P02769 (for amino acid sequences).

76 C. L. A. Geronimo and R. I. MacCuspie, *Microsc. Microanal.*, 2011, **17**, 206–214.

77 K. H. Hurst, K. M. N. Ansari, C. B. Roberts and W. R. Ashurst, *J. Microelectromech. Syst.*, 2011, **20**, 424–435.

78 K. Knop, R. Hoogenboom, D. Fischer and U. S. Schubert, *Angew. Chem., Int. Ed.*, 2010, **49**, 6288–6308.